



# Optimizing the Search for High- $z$ GRBs: The JANUS X-ray Coded Aperture Telescope

D. N. Burrows<sup>1,2</sup>, D. Fox<sup>1</sup>, D. Palmer<sup>3</sup>, P. Romano<sup>4</sup>, V. Mangano<sup>4</sup>, V. La Parola<sup>4</sup>,  
A. D. Falcone<sup>1</sup>, and P. W. A. Roming<sup>5</sup>

<sup>1</sup> Department of Astronomy and Astrophysics, The Pennsylvania State University, 525  
Davey Lab, University Park, PA 16802 USA

<sup>2</sup> e-mail: burrows@astro.psu.edu

<sup>3</sup> Los Alamos National Laboratory, Los Alamos, NM, USA

<sup>4</sup> Istituto Nazionale di Astrofisica – IASF-Palermo, Palermo, Italy

<sup>5</sup> Southwest Research Institute, San Antonio, TX, USA

**Abstract.** We discuss the optimization of gamma-ray burst (GRB) detectors with a goal of maximizing the detected number of bright high-redshift GRBs, in the context of design studies conducted for the X-ray transient detector on the *JANUS* mission. We conclude that the optimal energy band for detection of high- $z$  GRBs is below about 30 keV. We considered both lobster-eye and coded aperture designs operating in this energy band. Within the available mass and power constraints, we found that the coded aperture mask was preferred for the detection of high- $z$  bursts with bright enough afterglows to probe galaxies in the era of the Cosmic Dawn. This initial conclusion was confirmed through detailed mission simulations that found that the selected design (an X-ray Coded Aperture Telescope) would detect four times as many bright, high- $z$  GRBs as the lobster-eye design we considered. The *JANUS* XCAT instrument will detect 48 GRBs with  $z > 5$  and fluence  $S_x > 3 \times 10^{-7}$  erg  $\text{cm}^{-2}$  in a two year mission.

**Key words.** Instrumentation: miscellaneous – Stars: Gamma-ray burst: general – X-rays: Gamma-ray bursts – X-rays: Transients – X-rays: general – Gamma-rays: general

## 1. Introduction

One of the most compelling problems facing astrophysics in the early 21<sup>st</sup> century is to understand the early Universe, and in particular, the epoch known as the Cosmic Dawn (Blandford et al. 2010), when starlight from the first generations of stars reionized the neutral intergalactic medium, and when the struc-

ture of the Universe was set into the general patterns that still prevail today. Recent studies have shown that this reionization is complete around redshift  $z \sim 6$  (Fan et al. 2006). The Universe at such high redshifts is challenging to study, but progress has been rapid in recent years, with redshift records being broken repeatedly through a variety of techniques (e.g. Tanvir et al. 2009; Bouwens et al. 2010; Cucchiara et al. 2011) involving observations

---

Send offprint requests to: D. Burrows

of high- $z$  quasars, galaxies, and gamma-ray bursts (GRBs).

Each of these probes of the high- $z$  universe has strengths and weaknesses. Quasars are extremely luminous and can be bright sources even at high redshift, but the high UV and X-ray flux from the central engine strongly affects the properties of the host galaxy, making it atypical. Furthermore, the density of quasars drops rapidly at  $z > 6$ . Normal galaxies are being found, possibly at very high redshifts, in the Hubble Ultra Deep Field (e.g. Bouwens et al. 2010) through photometric dropouts. These photometric redshifts are not entirely reliable, as the dropouts can also be produced by dust extinction. More importantly, the galaxies being found represent the bright end of the luminosity distribution, and even so, are so faint that the spectroscopy needed to probe their gas is beyond the capabilities of current instrumentation. GRBs, on the other hand, probe star formation regions in all types of galaxies, and are so intrinsically bright that they can be used to probe the interstellar medium (gas and dust content) of host galaxies too faint to see, while the duration of the burst is short enough so that only gas in the immediate vicinity of the central engine is disturbed by the strong UV and X-ray emission. However, the short duration means that observations of GRBs must be carried out rapidly, before the GRB fades too much.

The use of GRBs as probes of distant galaxies has blossomed in the past six years (e.g. Prochaska et al. 2006; Vreeswijk et al. 2007; Prochaska et al. 2007; Tumlinson et al. 2007; Tejos et al. 2007; Prochaska et al. 2008; Chen et al. 2009; D’Elia et al. 2009; Levesque et al. 2010a,b), since the launch of the *Swift* satellite (Gehrels et al. 2004), which provides rapid arcsecond positions of GRBs. Still, after six years of operations, *Swift* has found only 3 GRBs with spectroscopic redshifts exceeding 6 (Table 1). The paucity of high- $z$  bursts found to date probably stems from several factors, one of which is almost certainly the long delay in obtaining the first indication of a high- $z$  event, which is typically many hours (Table 1). The key to finding more high- $z$  bursts is to design a satellite optimized to detect high- $z$  GRBs and

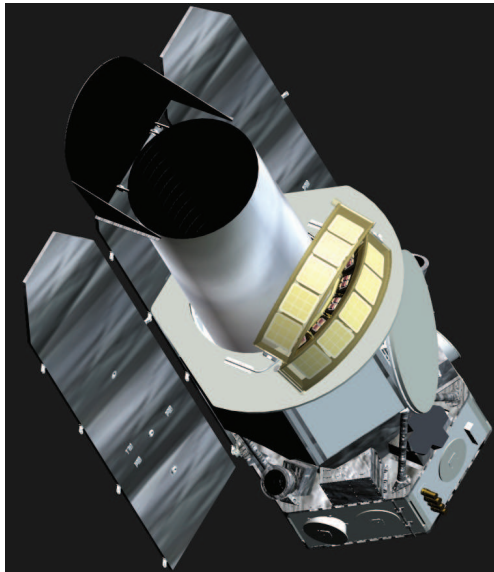


**Fig. 1.** *JANUS* design concept. The mission features an X-ray Coded Aperture Telescope (XCAT; gold-colored array of 10 modules mounted on the satellite top deck) to find GRBs and X-ray transients, and a Near Infrared Telescope (NIRT) that measures their redshifts with a low-resolution objective prism spectrometer.

to measure their redshifts within minutes. Here we discuss the optimization of an instrument, the X-ray Coded Aperture Telescope (XCAT), designed to find bright high- $z$  GRBs.

## 2. The X-ray Coded Aperture Telescope on the Joint Astrophysics Nascent Universe Satellite

The Joint Astrophysics Nascent Universe Satellite (*JANUS*; Burrows et al. 2010, see Fig. 1) is a proposed NASA Explorer mission optimized to study the Cosmic Dawn by finding high- $z$  GRBs and quasars and measuring their redshifts within minutes on-board. It has two main instruments: an X-ray Coded Aperture Telescope (XCAT) (Falcone et al. 2010) and a Near Infrared Telescope (NIRT). Here we discuss results of a trade study made for the XCAT instrument to maximize the

**Table 1.** Time delays to obtain redshift measurements for high- $z$  *Swift* GRBs

GRB	$z$	Type <sup>a</sup>	$T_P$	$T_S$	References
050904	6.295	S	10 hr	3.5 days	Cusumano et al. (2006); Tagliaferri et al. (2005), Kawai et al. (2006)
060116	6.6	P	41 hr	N/A	GCN Circ. 4545
080913	6.695	S	10 hr	11 hr	Greiner et al. (2009)
090423	8.2	S	7 hr	24 hr	Tanvir et al. (2009)
090429B	9.4	P	2.5 hr	N/A	Cucchiara et al. (2011)

<sup>a</sup>P = photometric redshift, S = spectroscopic redshift

$T_P$  = delay time to obtain photometric redshift;  $T_S$  = delay time to obtain spectroscopic redshift

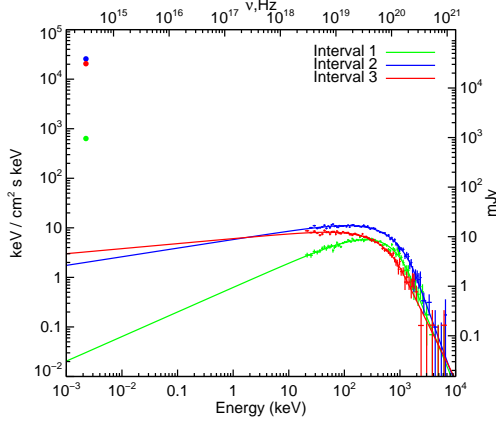


**Fig. 2.** Prompt emission spectra for GRB 080319B ( $z = 0.937$ ) for three time intervals, plotted as  $F_\nu$  in units of  $(\text{keV cm}^{-2} \text{s}^{-1} \text{keV}^{-1})$ . Although there is strong spectral evolution, the spectra from all three intervals are well-fit by a Band function (solid curves) with peak energy of a few hundred keV. From Racusin et al. (2008).

number of bright high- $z$  bursts that we can discover.

Traditionally, GRB detectors have operated in the hard X-ray to gamma-ray energy range, though *HETE-2* and *Beppo-SAX* both had soft X-ray capabilities. From previous studies, we know that the prompt emission from GRBs is typically characterized as a “Band function” (Band et al. 1993), an empirical function with a low energy power law that transitions smoothly

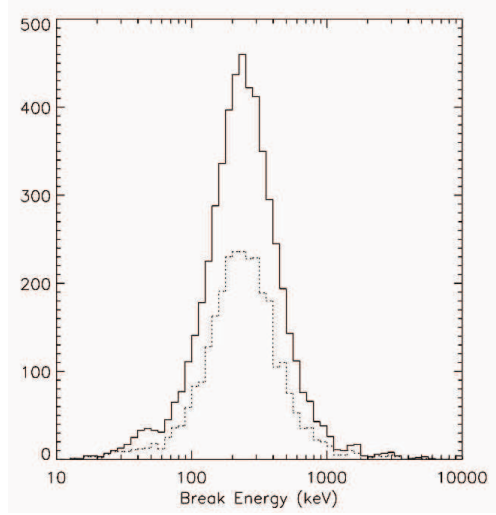


**Fig. 3.** Distribution of peak energies for BATSE bursts, from Preece et al. (2000).

to a high energy power law, with a peak energy ( $E_p$ , the peak in the  $\nu F_\nu$  spectrum) near the transition point. An example of time-resolved spectra of the prompt emission from a bright burst at  $z \sim 1$  is shown in Figure 2. The distribution of BATSE peak energies is shown in Figure 3: roughly 60% of the bursts have  $100 \text{ keV} < E_p < 600 \text{ keV}$ , with the most probable value at  $E_p \sim 220 \text{ keV}$ .

At high redshifts, the GRB prompt spectrum is shifted down in energy by a factor of  $(1 + z)$ . We can therefore expect that high red-

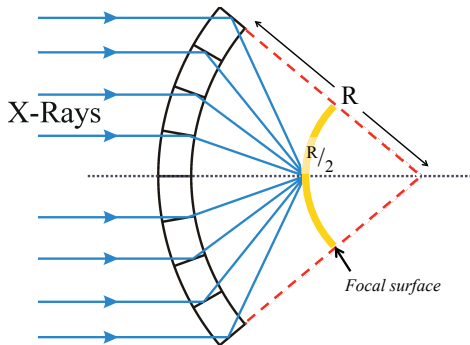


**Fig. 4.** Cartoon of lobster-eye optics. X-rays are reflecting at grazing incidence from planar surfaces arranged in a spherical pattern (a microchannel plate optic in this case). The thick yellow line represents the focal surface.

shift bursts will have peak energies in the tens of keV rather than the hundreds of keV. Below  $E_p$  the photon spectrum is typically  $I(E) \propto E^{-1}$  (photon index of  $\Gamma \sim -1$ ). Above the peak energy, the photon spectrum drops off rapidly with energy (typically as  $E^{-4.5}$ ), and observations at energies above  $E_p$  have poor sensitivity. Searches for high  $z$  bursts should therefore concentrate on the region below about 30 keV, where the number of photons per unit energy interval is high. Because the spectrum favors the soft X-ray bandpass, and because soft X-rays are much easier to detect than hard X-rays or  $\gamma$ -rays, a small, lightweight soft X-ray instrument can have better sensitivity to high- $z$  GRBs than a much larger, heavier hard X-ray or  $\gamma$ -ray instrument, and is better suited to small missions in the SMEX or EX class.

### 2.1. Wide-Field X-Ray Imaging

Techniques available for performing wide angle X-ray transient surveys are severely restricted. Large fields of view can be monitored with scanning collimator instruments (such as the *Uhuru* satellite or the *MAXI* mission), but these typically have poor position determination accuracy (of order tens of arcminutes) that is insufficient to localize GRBs and other transients well enough to identify optical counterparts. They also typically miss short tran-

sients like most GRBs. There are no materials with sufficient transparency and refractive power available to make conventional lenses such as those used in optical cameras. Large fields of view are feasible using multilayer-coated mirrors at normal incidence (e.g. Smith et al. 1990), which work by constructive interference of X-rays from layers of alternating high-and-low  $Z$  materials, but these mirrors have very narrow bandpasses and cannot be used for broad-band studies. Broad-band X-rays can only be reflected at grazing incidence, making the construction of conventional wide field optics virtually impossible. The relatively large grazing angles needed for wide fields of view also limit the bandpass, since the maximum grazing angle is inversely proportional to the photon energy. The standard astronomical X-ray telescope uses a Wolter I design (Wolter 1952a,b) that typically has fields of view less than a degree in diameter, with strong vignetting near the edges of the field of view.

These problems can be solved through the use of lobster-eye optics, using a curved grazing incidence optic in which each segment concentrates light from a different direction on the sky, but all reflections are at grazing incidence (Figure 4). Such designs have been under development for more than a decade, utilizing micropore optics or other systems of reflectors (e.g. Angel 1979; Fraser et al. 2002; Pearson et al. 2003; Švéda et al. 2009; Tichý et al. 2009; Putkunz & Peele 2009). Lobster-eye designs have several disadvantages, including a complex Point Spread Function (PSF; see Figure 5 or Hudec et al. (2004)), small bandpass due to the reflective optics, a complex energy-dependent effective area curve (e.g., Figure 7), and relatively heavy optics. Nevertheless, the sensitivity to point sources is superior to coded apertures (discussed below). Lobster-eye designs, however, have limited flight heritage.

For continuous, wide-field-of-view, broad-band, X-ray imaging with arcminute position determination, only coded aperture imaging has significant flight history. Since 1972, approximately two dozen imaging coded aperture astronomical telescope designs have flown in space or on balloons (see <http://astrophysics.gsfc.nasa.gov/cai>). Most in-

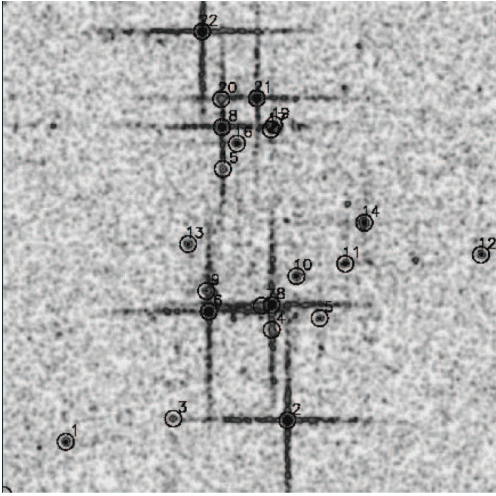


**Fig. 5.** Simulation of an observation of a  $10^\circ \times 10^\circ$  region of the LMC with the *LOBSTER-ISS* instrument (1 day exposure). From Fraser et al. (2002). The square pore optics produce a cruciform PSF.

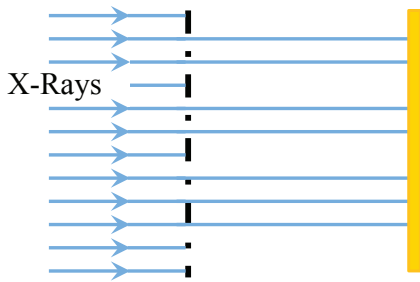


**Fig. 6.** Cartoon of coded aperture “optics”. X-rays are either transmitted or absorbed by cells in the mask (black) before impinging on the detector plane (yellow). We use a 2-D random mask pattern to suppress ghost images.

struments designed to detect GRBs have used 1-D or 2-D coded aperture masks, using techniques developed and discussed by a number of authors including Dicke (1968); Fenimore & Cannon (1978); Proctor et al. (1979) and Caroli et al. (1987). Coded aperture masks work as multiple pinhole cameras or shadow masks (Figure 6). Each point source in the field of view casts a shadow of the mask pattern onto the detectors. As the angle of the source

varies on the sky, the shadow on the detectors is offset accordingly. By deconvolving the detector event pattern with the mask pattern, an image of the sky can be obtained. Two dimensional coded apertures provide more robust positions on the sky than perpendicular 1-D coded apertures (which can sometimes provide only a 1-D position and which sometimes have ghost images). The 2D coded mask, combined with sophisticated triggering algorithms, gives the *Swift* BAT instrument an extremely low false burst rate of just a few percent. Coded aperture instruments are in general less sensitive than lobster-eye instruments because the photons are not concentrated into images, and because every source and all diffuse emission contribute noise to every pixel on the detector. Nevertheless, coded aperture instruments have advantages in terms of broad-band performance and extremely wide fields of view for a given mass.

Three designs were considered in detail in our trade studies for *JANUS*: a lobster-eye design similar to the *LOBSTER-ISS* instrument proposed a decade ago for flight on the International Space Station (Fraser et al. 2002); a monolithic coded aperture design similar to the *Swift* BAT, with a single large mask imaging onto a single focal plane detector array; and a modular coded aperture design, in which each module pointed in a different direction (X-ray Coded Aperture Telescope, or XCAT). We found that sensitivity limits for monolithic and modular coded aperture instruments are similar for on-axis sources, but that the modular design performs better at the edges of the field of view (less vignetting) and provided more design flexibility for accommodating multiple instruments on a small platform. We then compared the lobster-eye concept to the modular coded aperture. Instrument parameters for the two design concepts we considered are given in Table 2, and effective area curves are shown in Figure 7. Instrument mass and volume constraints limited the size of both instruments; the lobster-eye design considered here is larger (larger focal length) and more massive than XCAT, and covers only 7% of the solid angle of the XCAT instrument, but is much more sensitive.

**Table 2.** Comparison of coded aperture and lobster-eye designs

Instrument	XCAT (coded aperture)	Lobster-eye
Energy Range (keV)	0.5–20	0.3–3
Imaging technique	2-D coded mask	Lobster-eye grazing incidence
FOV (sr)	3.9	0.26
Mask/Optics area (cm <sup>2</sup> )	1690	1600
Focal length	158 mm	> 350 mm
Angular resolution (arcmin)	6.3	4
Focal Plane Area (cm <sup>2</sup> )	147	400
Detector type	H2RG HyViSI CMOS	GEM
Power	70 W	51 W
Mass	57 kg	95 kg
Limiting sensitivity in 30 s (mCrabs)	240 (6.5 $\sigma$ )	2.7 (5 $\sigma$ )
# GRBs in 2 years with $5 < z < 12$ and $S_x > 3 \times 10^{-7}$ erg cm <sup>-2</sup>	48	11

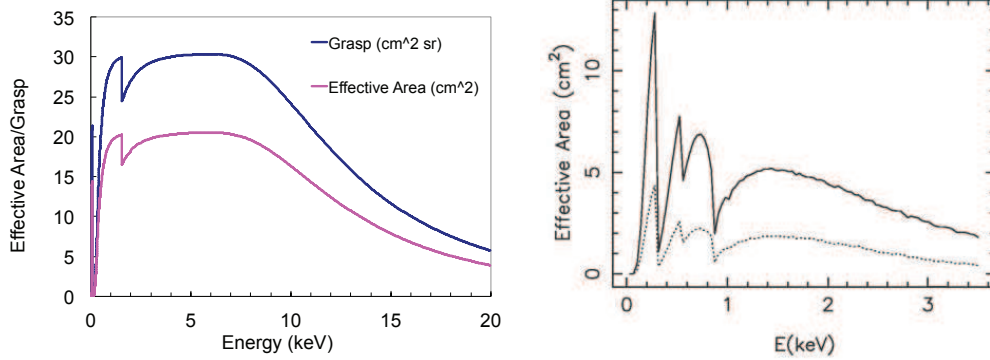


**Fig. 7.** Left: XCAT grasp and effective area curves for a single module. Right: LOBSTER-ISS effective area curve (from Fraser et al. 2002). The dotted curve shows the effective area for the central true focus, while the solid curve includes area scattered into the cruciform arms. The XCAT effective area curve is much broader and simpler because the coded mask cells are either transparent or opaque over most of the energy range of the detector, so the curve is dominated by the detector quantum efficiency. The LOBSTER-ISS curve has strong features caused by the grazing incidence reflections off of the Ni-coated optic, and has a much narrower bandpass.

### 3. Simulations

#### 3.1. JANUS Mission Simulation

Our detailed simulation began with a simulation of the mission geometry for *JANUS*. The *JANUS* mission will spend most of its time surveying nearly 1/2 of the high-latitude sky. The *JANUS* team produced a list of fields cov-

ering the northern and southern galactic caps, and developed an algorithm to select fields for observation. A detailed mission simulation was constructed that included realistic orbital parameters and spacecraft design parameters, and calculated the position of the spacecraft every minute for a two year mission. At each one minute time step, the spacecraft field



of view was compared against observing constraints (keep-out zones around the Sun, Moon, and Earth). When one of these constraints impinged on the field of view, a new target was selected that would be observable for at least ten minutes, and the spacecraft slewed to the new target (using realistic slew times based on a detailed model of the spacecraft’s attitude control system). The simulation correctly accounted for time spent in the South Atlantic Anomaly (where the instruments cannot observe due to high background rates), and included interruptions to the mission timeline for GRBs that were injected at random times using the expected GRB event rate. The mission simulation demonstrated that *JANUS* can complete its quasar survey in a two year mission with considerable margin, and served as the basis for our detailed simulation of the XCAT instrument performance.

### 3.2. XCAT GRB Simulation

To predict *JANUS* burst rates as a function of redshift, we carried out a rigorous simulation of XCAT performance on-orbit, making use of the *JANUS* mission simulation to provide a realistic history of live-time periods and satellite pointings (including relative Earth position, to account for partial occultation of the XCAT FOV). To generate an appropriate population of GRBs for detection, we used the best-fit luminosity and redshift distributions from Wanderman & Piran (2010), as updated on the web to reflect the latest Swift results. We drew burst redshifts ( $0 < z < 30$ ) and luminosities ( $L_{peak} \geq 10^{50} \text{ erg s}^{-1}$ ) from these distributions at Poissonian intervals according to the known all-sky rate, placed the burst at a random position on the sky, and compared to the FOVs of the 10 XCAT modules (from the mission simulation). If the burst was in view of one or more modules, then a simulated burst light curve (with Poisson noise) was generated for each viewing module – including contributions from all point X-ray sources in the module’s FOV along with the known diffuse X-ray and particle backgrounds – and was fed to the XCAT triggering software. If the burst resulted in a trigger, the properties of the burst were

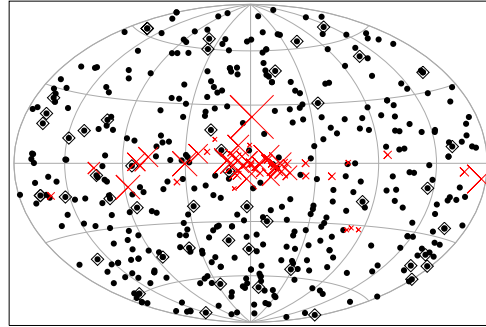


**Fig. 8.** Distribution of simulated GRBs on the sky for the XCAT instrument design (2 year mission). Black diamonds indicate the high- $z$  GRBs. Red crosses show the location of the 50 brightest X-ray sources seen by the *RXTE* All-Sky Monitor (ASM); the 263 sources detected by the ASM during the week of 7 February 2009 were included as background sources in the simulation. (Cross size indicates relative source brightness.)

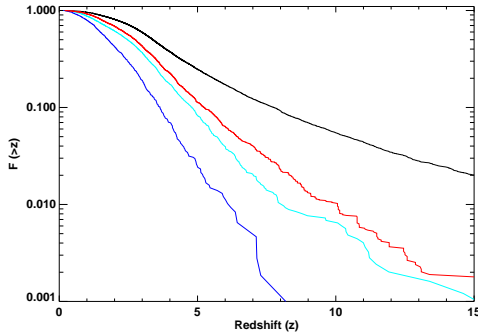
recorded. These successful triggers formed the basis for our predicted redshift distribution. To minimize Poisson uncertainties due to the Monte Carlo nature of the simulation, we carried out 20 runs of 400 days (on-orbit) duration each.

Burst light curves were simulated by rescaling the Swift BAT (15–150 keV) light curves of bursts with known redshifts to the (new and distinct) redshift and peak luminosity of the simulated burst, and extrapolating the observed burst spectrum to the lower energy range of XCAT. (For simulated high- $z$  bursts this extrapolation is minimal, since the median redshift for the Swift burst sample is only  $z = 2.3$ ). We have developed a library of 111 Swift BAT light curves for this purpose.

On the basis of the simulations, we predict a mean burst detection rate of 0.7 GRBs per day with XCAT. The distribution of these bursts on the sky is shown in Figure 8. The redshift distribution of detected bursts is given in Table 3 and is shown in Figure 9. Beyond  $z = 12$  the Ly $\alpha$  break redshifts beyond the NIRT bandpass so that a redshift measurement is not possible. The XCAT design will detect 61 bursts with  $z > 5$  in a 2 year mission.

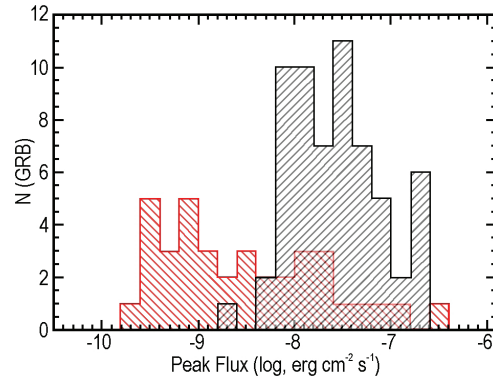
**Table 3.** Redshift Distribution of Simulated *JANUS* GRBs (2 year mission)

$z$	5	6	7	8	9	10	11	12
$f(> z)$	12%	6.4%	3.4%	1.8%	0.9%	0.4%	0.1%	0.16%
$N(> z)$	61	33	17	9	5	2	1	1

**Fig. 9.** Redshift distribution of GRBs. The black line shows the distribution of the parent population from Wanderman & Piran (2010). The red line shows the results of our simulation for the XCAT instrument. The cyan line shows the distribution for the *Swift* BAT instrument. The dark blue line shows the distribution for BATSE. We expect XCAT to detect a significantly higher fraction of high- $z$  GRBs than *Swift*; this, combined with rapid redshift measurements for every high- $z$  GRB detected by XCAT, will result in about 30 GRBs per year with  $z > 5$ .

### 3.3. Lobster-Eye Simulation

The GRBs generated during the detailed XCAT simulation were also used as input to a simulation of the lobster-eye design. The instrument parameters used for the simulation are shown in Table 2. We found that the lobster-eye instrument detected about the same total number of bursts in spite of its small field of view, because the improved sensitivity allowed it to detect every GRB that went off in its field of view. Although the total number of bursts is similar, the distribution of peak flux is very different from that of the XCAT instrument (Figure 10).

**Fig. 10.** Distribution of peak fluxes of high-redshift GRBs ( $5 < z < 12$ ) detected by XCAT (black) and the lobster-eye design considered here (red). The two instruments detect similar numbers of high- $z$  GRBs, but the XCAT distribution is much brighter.

### 3.4. Optical / Gamma-ray Correlation

This difference in peak flux distributions of the high redshift burst samples detected by XCAT and by our lobster-eye implementation is quite significant. Previous studies have shown that the brightness of the optical afterglow is correlated with the brightness of the prompt  $\gamma$ -ray emission (Gehrels et al. 2008; Nysewander et al. 2009; Kann et al. 2010). Although there is considerable scatter (perhaps due to dust extinction affecting the optical brightness), the trend is that brighter GRBs (measured by peak flux, total fluence, or total isotropic energy output) have brighter optical afterglows. Bright afterglows are essential for detailed high resolution studies of the host galaxies of the bursts. *Therefore, in order to use high redshift bursts to probe galaxies at the Cosmic Dawn, one should optimize the burst detection to maximize the number of bright bursts.* We find that



the XCAT design will detect 24 high-z GRBs per year at fluence  $S_x > 3 \times 10^{-7}$  erg cm<sup>-2</sup>, while the lobster-eye design detects only 6 per year.

#### 4. Conclusions

Our detailed simulations confirmed our “back-of-the-envelope” determination that high-z GRBs are best detected in the soft X-ray band, by which we mean energies of roughly 0.5–20 keV. In this energy band, the best options for wide-field transient detectors are lobster-eye and coded aperture designs. The lobster eye design is more sensitive and will find more faint X-ray transients, but its field of view is too small to find many rare, bright, high-z GRBs that can be used to probe galaxies in the era of the Cosmic Dawn with high resolution spectroscopy followup. The XCAT coded mask design was selected for the *JANUS* mission because it is optimized to find these high-z bursts, and therefore provides the best solution to the prime *JANUS* science goals of probing the Cosmic Dawn with GRBs and quasars.

#### References

- Angel, J. R. P. 1979, *ApJ*, 233, 364
- Band et al., D. 1993, *ApJ*, 413, 281
- Blandford, R., Hillenbrand, L., Haynes, M. P., et al. 2010, *New Worlds, New Horizons in Astronomy and Astrophysics* (The National Academies Press, ISBN-10: 0-309-15799-4)
- Bouwens, R. J., Illingworth, G. D., Oesch, P. A., et al. 2010, *ApJ*, 709, L133
- Burrows, D. N., Roming, P. W. A., Fox, D. B., et al. 2010, in *Society of Photo-Optical Instrumentation Engineers (SPIE) Conference Series*, Vol. 7732, *Space Telescopes and Instrumentation 2010: Ultraviolet to Gamma Ray*, 77321U–77321U–10
- Caroli, E., Stephen, J. B., Di Cocco, G., Natalucci, L., & Spizzichino, A. 1987, *Space Sci. Rev.*, 45, 349
- Chen, H.-W., Perley, D. A., Pollack, L. K., et al. 2009, *ApJ*, 691, 152
- Cucchiara, A., Levan, A. J., Fox, D. B., et al. 2011, ArXiv e-prints
- Cusumano, G., Mangano, V., Chincarini, G., et al. 2006, *Nature*, 440, 164
- D’Elia, V., Fiore, F., Perna, R., et al. 2009, *A&A*, 503, 437
- Dicke, R. H. 1968, *ApJ*, 153, L101+
- Falcone, A. D., Burrows, D. N., Barthelmy, S., et al. 2010, in *Society of Photo-Optical Instrumentation Engineers (SPIE) Conference Series*, Vol. 7732, *Space Telescopes and Instrumentation 2010: Ultraviolet to Gamma Ray*, 77324F–74324F–7
- Fan, X., Strauss, M. A., Becker, R. H., et al. 2006, *AJ*, 132, 117
- Fenimore, E. E. & Cannon, T. M. 1978, *Appl. Opt.*, 17, 337
- Fraser, G. W., Brunton, A. N., Bannister, N. P., et al. 2002, in *Society of Photo-Optical Instrumentation Engineers (SPIE) Conference Series*, ed. K. A. Flanagan & O. H. W. Siegmund, Vol. 4497, 115–126
- Gehrels, N., Barthelmy, S. D., Burrows, D. N., et al. 2008, *ApJ*, 689, 1161
- Gehrels, N., Chincarini, G., Giommi, P., et al. 2004, *ApJ*, 611, 1005
- Greiner, J., Krühler, T., Fynbo, J. P. U., et al. 2009, *ApJ*, 693, 1610
- Hudec, R., Švéda, L., Inneman, A., & Pina, L. 2004, in *Society of Photo-Optical Instrumentation Engineers (SPIE) Conference Series*, ed. G. Hasinger & M. J. L. Turner, Vol. 5488, 449–459
- Kann, D. A., Klose, S., Zhang, B., et al. 2010, *ApJ*, 720, 1513
- Kawai, N., Kosugi, G., Aoki, K., et al. 2006, *Nature*, 440, 184
- Levesque, E. M., Berger, E., Kewley, L. J., & Bagley, M. M. 2010a, *AJ*, 139, 694
- Levesque, E. M., Bloom, J. S., Butler, N. R., et al. 2010b, *MNRAS*, 401, 963
- Nysewander, M., Fruchter, A. S., & Pe’er, A. 2009, *ApJ*, 701, 824
- Pearson, J. F., Bannister, N. P., Fraser, G. W., & The Lobster-ISS Consortium. 2003, *Astronomische Nachrichten*, 324, 168
- Preece, R. D., Briggs, M. S., Mallozzi, R. S., et al. 2000, *ApJS*, 126, 19
- Prochaska, J. X., Chen, H.-W., & Bloom, J. S. 2006, *ApJ*, 648, 95
- Prochaska, J. X., Chen, H.-W., Dessauges-

- Zavadsky, M., & Bloom, J. S. 2007, *ApJ*, 666, 267
- Prochaska, J. X., Dessauges-Zavadsky, M., Ramirez-Ruiz, E., & Chen, H.-W. 2008, *ApJ*, 685, 344
- Proctor, R. J., Skinner, G. K., & Willmore, A. P. 1979, *MNRAS*, 187, 633
- Putkunz, C. T. & Peele, A. G. 2009, *Optics Express*, 17, 14156
- Racusin et al., J. L. 2008, *Nature*, 455, 183
- Smith, B. W., Bloch, J. J., & Roussel-Dupre, D. 1990, *Optical Engineering*, 29, 592
- Tagliaferri, G., Antonelli, L. A., Chincarini, G., et al. 2005, *A&A*, 443, L1
- Tanvir, N. R., Fox, D. B., Levan, A. J., et al. 2009, *Nature*, 461, 1254
- Tejos, N., Lopez, S., Prochaska, J. X., Chen, H.-W., & Dessauges-Zavadsky, M. 2007, *ApJ*, 671, 622
- Tichý, V., Hromčík, M., Hudec, R., et al. 2009, in *Society of Photo-Optical Instrumentation Engineers (SPIE) Conference Series*, Vol. 7360
- Tumlinson, J., Prochaska, J. X., Chen, H.-W., Dessauges-Zavadsky, M., & Bloom, J. S. 2007, *ApJ*, 668, 667
- Švéda, L., Hudec, R., Pina, L., Semencova, V., & Inneman, A. 2009, in *Society of Photo-Optical Instrumentation Engineers (SPIE) Conference Series*, Vol. 7360
- Vreeswijk, P. M., Ledoux, C., Smette, A., et al. 2007, *A&A*, 468, 83
- Wanderman, D. & Piran, T. 2010, *MNRAS*, 406, 1944
- Wolter, H. 1952a, *Annalen der Physik*, 445, 94
- Wolter, H. 1952b, *Annalen der Physik*, 445, 286